Dielectrically Loaded Quad-Ridge Flared Horn for Beamwidth Control Over Decade Bandwidth-Optimization, Manufacture, and Measurement

Dielectrically Loaded Quad-Ridge Flared Horn for Beamwidth Control Over Decade Bandwidth—Optimization, Manufacture, and Measurement

Jonas Flygare, *Student Member, IEEE*, and Miroslav Pantaleev

***Abstract*— We present the design, manufacture, and measured performance of a dielectrically loaded quad-ridge flared horn (QRFH) feed for decade bandwidth radio astronomy application. The introduction of the dielectric load improves the QRFH beamwidth control in H-plane at the mid and upper frequency range. Consequently on the reflector, illumination efficiency, phase efficiency, and the intrinsic cross-polarization ratio (IXR) have been improved. The dielectric load is made from homogeneous low-loss polytetrafluoroethylene and has a low profile with a cylinder shape for simple installation at the center of the QRFH. The dielectrically loaded QRFH presented here covers 1.5–15.5 GHz with a calculated average aperture efficiency above 50% on a f/D = 0.3 prime-focus reflector. We present a calculation of system noise temperature and sensitivity for the QRFH on a 100 m prime-focus reflector. Measured beam patterns of the QRFH are in good agreement with the simulations over the full frequency band. The input reflection coefficient was predicted to be below −10 dB across the bandwidth. We present a tolerance analysis that explains why the measured one deviates.**

***Index Terms*— Dielectric materials, quad-ridge flared horn (QRFH), radio astronomy, reflector feed, ultra wideband (UWB) antennas.**

I. Introduction

ULTRA wideband (UWB) systems enable science projects in radio astronomy to have a large continuous bandwidth. UWB systems can reduce the number of receivers needed to cover a large frequency band. For large arrays with hundreds of reflector telescopes, such as the Square Kilometer Array (SKA) [1], the Allen Telescope Array (ATA) [2], and the Next Generation Very Large Array (ngVLA) [3], UWB systems could reduce manufacture and operations costs. The project Broadband (BRAND) [4] is to develop an UWB receiver from *L*- to *Ku*-band with one single feed [5].

For wideband receivers a key challenge is to keep the feed's beamwidth constant across the wide frequency range in order to illuminate the reflector, with low spill-over noise and high aperture efficiency over the whole band. Some feeds can achieve symmetric beam patterns with constant beamwidth over a narrow band [6]. Low-noise amplifiers (LNA) are easy to impedance match over a narrow band. However, the current state-of-the-art LNA technology can achieve low noise temperatures over wide bandwidths [7], [8]. Therefore, feed beamwidth control needs to be improved to push UWB receiver's sensitivity closer to that of narrowband systems. Different types of UWB feeds have been explored for radio astronomy: Eleven Feed [9], [10]; Antonio Feed [2]; quasi-self-complementary feed (QSC) [11]; and quad-ridge flared horn (QRFH) [12], [13]. The QRFH is generally made entirely from low-loss metal and with a robust structure. The QRFH ridges achieve dual-linear polarization without the need of an orthomode transducer (OMT). QRFHs can be designed for two 50 Ω single-ended ports with input reflection coefficients typically less than −10 dB over 6:1 bandwidth with succesful prototypes up to 50 GHz [14]. The QRFH robustness, single-ended interface and compact design leads to simple integration in a cryostat dewar together with the LNAs for low-noise applications. The waveguide property of QRFHs mitigate radio frequency interference (RFI) below the cutoff frequency.

In this article we demonstrate how the QRFH beamwidth control can be improved over 10:1 bandwidth with a dielectric load. This technique has achieved good beam pattern symmetry over 6:1 bandwidth with a three-layered dielectric [15]. We present a simpler low-profile uniform-dielectric cylinder for decade bandwidth. This work adds to the understanding

(a) (b)

Fig. 1. (a) Dielectrically loaded QRFH. (b) Dielectric load.

Manuscript received November 20, 2018; revised August 19, 2019; accepted August 21, 2019. Date of publication September 30, 2019; date of current version January 3, 2020. The project leading to this publication has received funding from the European Union's Horizon 2020 research and innovation programme under grant agreement No 730562 [RadioNet]. *(Corresponding author: Jonas Flygare.)*

J. Flygare is with the Onsala Space Observatory, Department of Space, Earth and Environment, Chalmers University of Technology, SE-41296 Gothenburg, Sweden (e-mail: jonas.flygare@chalmers.se).

M. Pantaleev is with the RUAG Space, CH-8052 Zürich, Switzerland (e-mail: miroslav.pantaleev@gmail.com).

Color versions of one or more of the figures in this article are available online at http://ieeexplore.ieee.org.

Digital Object Identifier 10.1109/TAP.2019.2940529

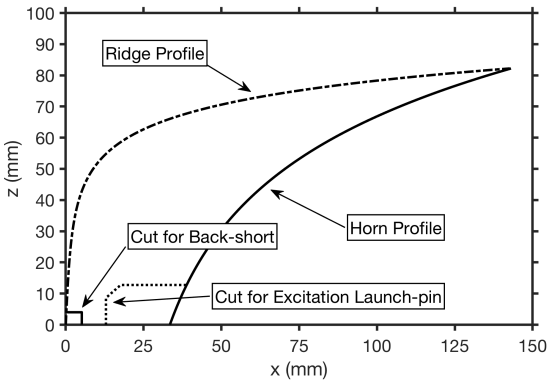

Fig. 2. Exponential profiles of the QRFH horn and ridges.

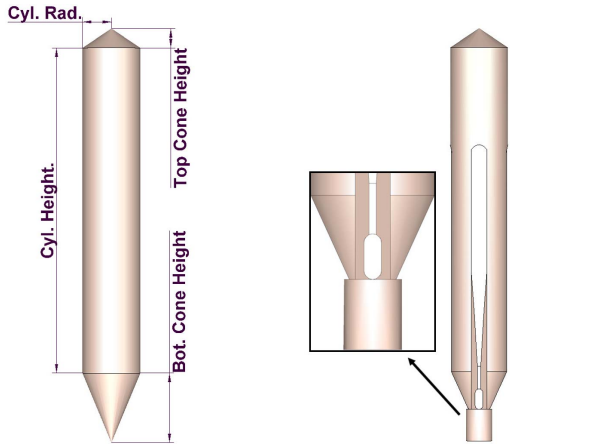

Fig. 3. Dielectric load: (Left) The four parameters for optimization. (Right) Final model with cylindrical base for support, trace for ridges and hole for launch-pins.

of QRFH design, [12]– [16], and the technique of dielectric loading of horn antennas [17], [18]. The novelty and contributions in this article are: 1) simple low-profile dielectric load made from homogeneous low-loss material with an easy installation in the QRFH; 2) optimization, manufacture, and measurement of the dielectrically loaded QRFH covering, see Fig. 1, 1.5–15.5 GHz, designed for a $f/D = 0.3$ reflector; and 3) tolerance analysis of the QRFH excitation point for manufacturing.

II. Feed Design

A. Quad-Ridge Flared Horn

The two profiles that make up the QRFH structure (horn and ridge shape) can be defined through: analytical expressions [12], [13]; spline-defined profiles [16], [19]; or a combination. We use a well-known exponential expression to optimize for this QRFH application. The two profiles are defined in width $x(z)$ as a function of height z, each with a separate set of five parameters according to

$$x(z) = A\left(\frac{r_a - r_t}{e^{RL}-1}e^{Rz} + \frac{r_t e^{RL} - r_a}{e^{RL}-1}\right) + (1-A)\left(r_t + (r_a - r_t)\frac{z}{L}\right) \quad (1)$$

where r_t and r_a defines the throat and aperture radius respectively. L is the taper length, with an exponential opening rate R. The linear contribution in each taper is defined by A. The two profiles are joined together by the shared endpoint at the aperture of the horn and hence two parameters are shared between them. Fig. 2 illustrates the profiles of the horn and the ridges. The back-short section is defined as a rectangular cut in the ridge's bottom. The minimum distance between orthogonal adjacent ridges at the feeding point is parametrized by a 45° chamfer cut, for details see Fig. 5(e). The horn is excited in the bottom part by two orthogonal 50 Ω single-ended launch-pins to achieve dual-polarization. In total there are 12 optimization parameters for the metallic structure of the QRFH. The horn profile was modified in the bottom part in order to reduce the drilled hole depth for the excitation launch-pins, as illustrated in Fig. 2. This radial reduction at the bottom has no significant effect on the feed performance.

B. Dielectric Load

The dielectric load has a simple cylindrical structure, defined from three geometric shapes—cone/cylinder/cone—in a solid homogeneous material. This results in four parameters for optimization: the bottom cone height, the cylinder height, the cylinder radius; and the top cone height, illustrated in Fig. 3.

C. Optimization

The dielectrically loaded QRFH was optimized in two steps to illuminate a $f/D = 0.3$ axisymmetric prime-focus reflector with equivalent half-subtended angle $\theta_e = 79.6°$. The first step was performed with CST Microwave Studios to find a promising feed model with near-constant beamwidth over the frequency range 1.5–15.5 GHz. For E-plane ($\phi = 0°$), the goal was to achieve a half 12 dB beamwidth within [75°, 85°]. For the H-plane ($\phi = 90°$) the goal was a half 12 dB beamwidth larger than 50°. The goal for the input reflection coefficients (S_{11}, S_{22}) was to be below −10 dB. The goals were set to be achieved across the bandwidth. The most promising feed model based on these goals was selected for the second step. In the second step, a MATLAB/CST-script was used which calculates the sub-efficiencies for each iteration of the feed in the prime-focus reflector [20]. The goal was set to achieve an aperture efficiency average better than 50% across the bandwidth and input reflection coefficients below −10 dB. The particle swarm optimization (PSO) algorithms provided in CST and MATLAB were used for the two optimization steps respectively. For the best model found, aperture efficiency and beam patterns on the reflector was confirmed with TICRA's GRASP software using physical optics (PO) and physical theory of diffraction (PTD). In the optimization, a total of 18 parameters were included: 12 for the QRFH ridges and horn shape, four for the dielectric load shape, and two for the launch-pin's height positions in the horn. The final optimized values of the 18 parameters are presented in Table I. The total number of optimization runs was eight with 1500–5000 iterations in each run. The variable search space was altered in size between

TABLE I

FINAL PARAMETER VALUES OF THE OPTIMIZED FEED, SUBSCRIPTS H AND R INDICATE HORN AND RIDGE RESPECTIVELY

Parameter	Value	Parameter	Value
R_{H}	0.030	R_{R}	0.093
A_{H}	0.944	A_{R}	0.978
$r_{\mathrm{a;\,H}}$ (=$r_{\mathrm{a;\,R}}$)	143.20 mm	L_{H} (=L_{R})	82.20 mm
$r_{\mathrm{t;\,H}}$ ($r_{\mathrm{t;\,R}}$=0.1 mm, fix)	33.50 mm	Ridge thickness	2.00 mm
Back-short height	4.00 mm	Adjacent ridges dist.	0.49 mm
Back-short width	5.25 mm	Opposite ridges dist.	1.10 mm
Diel. cylinder radius	3.75 mm	Diel. bot. cone height	8.80 mm
Diel. cylinder height.	41.20 mm	Diel. top cone height	2.50 mm
Launch-pin 1, z-coord.	5.00 mm	Launch-pin 2, z-coord.	5.60 mm

the runs where the first run allowed the largest search space. The dielectric load material was fixed during optimization to be homogeneous polytetrafluoroethylene (PTFE or "Teflon") with relative permittivity of $\epsilon_r = 2.1$. PTFE was chosen due to the known coefficient of thermal expansion at cryogenic temperatures with low expected shrinkage. PTFE also has a low cost and it is possible to machine it using computer controlled numerical (CNC) machining.

III. MECHANICAL DESIGN AND MANUFACTURE

The QRFH is manufactured as four quarters of the horn with the inner profile CNC-machined and the details on the outside with electrostatic discharge machining (EDM), see Fig. 4(b) and (c) respectively. The ridges are CNC-machined and clamped between the quarters, with steering pins to align the structure. The horn quarters and ridges are contacted with screws along the profile, see Fig. 4(c). The bottom of the horn consists of four block-pieces that clamp the back-short of the horn and they are steered into place with a bottom lid. The bottom-lid is screwed all the way through the four block-pieces into the bottom of the four quarters of the horn for contact, see Fig. 4(d). The QRFH is 87 mm in height and 292 mm in aperture diameter with 2 mm thick ridges, all manufactured in Aluminum. The dielectric load is CNC-machined in PTFE material with a cylindrical base, see right-hand side of Figs. 3 and 4(e). The cylinder base adds support to the dielectric load from the bottom-lid for alignment in boresight. The hole in the lower part of the dielectric load is 2.5 mm in height and 1 mm in width to allow room for the launch-pins to pass through. The traces seen in the sides of the dielectric load matches the ridges' shape to fit in-between. In Fig. 4(a) the assembly structure of the QRFH (without launch-pins) is presented with the dielectric load seen in the center. The dielectric load is clamped between the ridges and the back-short so that it cannot move, as shown in Fig. 5(f). The dielectric load can easily be installed or removed by detatching one half of the horn structure. Unlike [15] and [18], the dielectric load we suggest has a low profile, 52.5 mm in height and 7.5 mm in diameter, which does not extend beyond the horn aperture. Because of this, the horn aperture can be installed close to the aperture of the cryostat dewar. It is common that the dewar's vacuum window curve inward because of the pressure differential. If the distance from dewar to horn aperture is too large, it can cause resonant effects inside the dewar for a low-gain horn with a wide beam. The alternative to make the vacuum window larger in diameter would load the cryostat with unwanted infrared (IR) radiation and increase the power consumption.

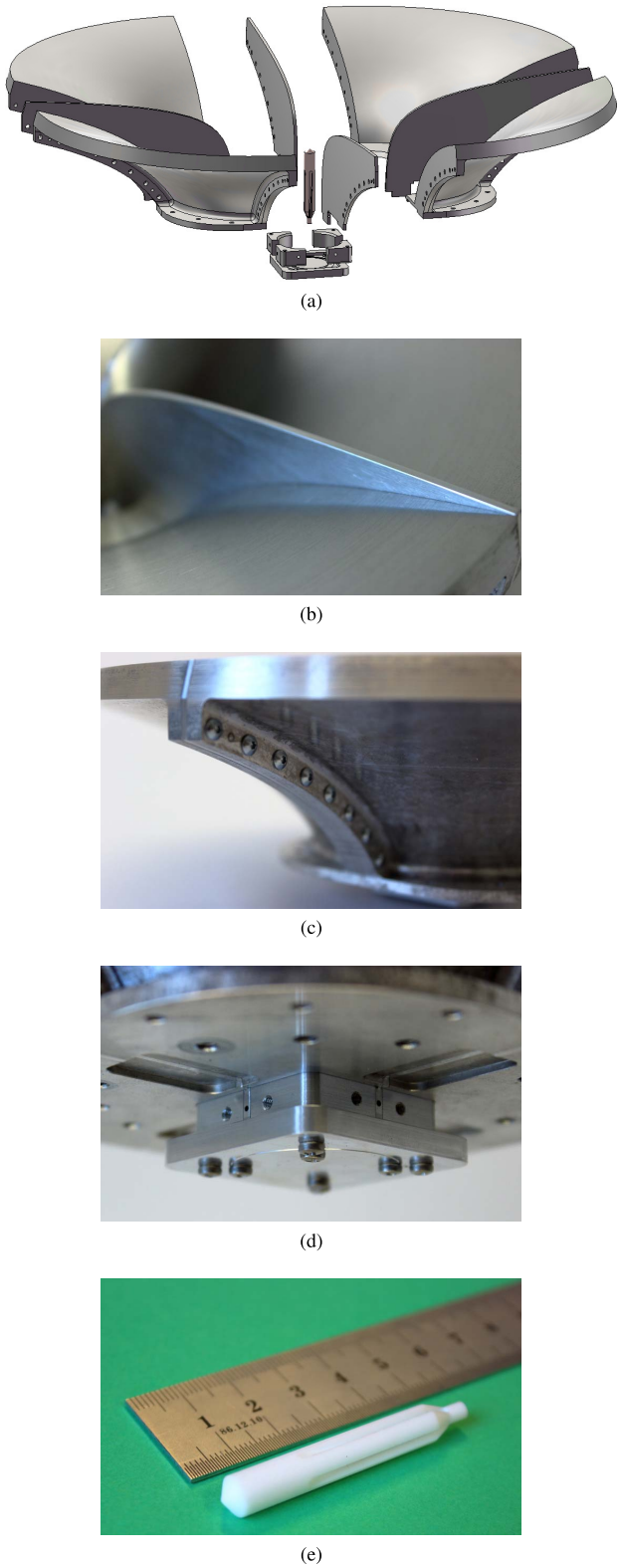

(a) (b) (c) (d) (e)

Fig. 4. Manufactured QRFH. (a) Assembly view. (b) Ridge clamped between quarters. (c) Screws along quarter. (d) Bottom of horn, launch-pin's holes. (e) Dielectric load (cm-ruler).

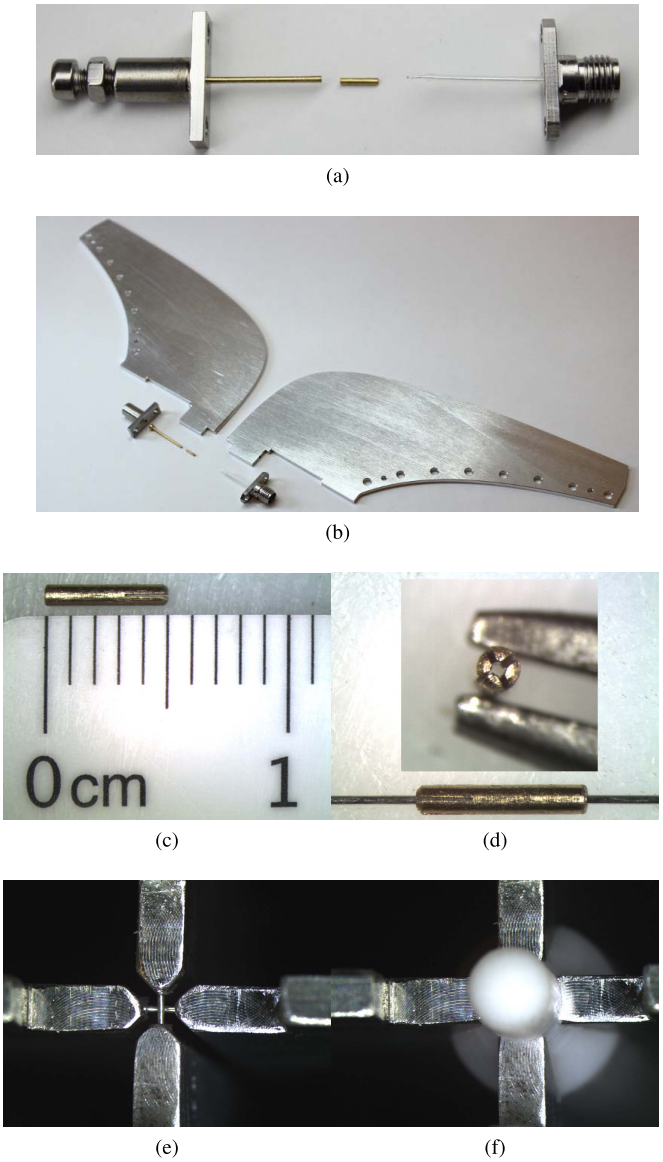

(a) (b) (c) (d) (e) (f)

Fig. 5. QRFH excitation. (a) Screw with push-pin, chuck connector, launch-pin to SMA. (b) Ridges, launch-pin setup. (c) Chuck connector. (d) Chuck opening, threaded on 0.287 mm pin. (e) Launch-pins installed. (f) Dielectric load installed.

By using a low-profiled dielectric load, the QRFH footprint is not affected. The small dimensions of the dielectric load also mitigates the risk of strong thermal gradients inside the material. Thermal contact for cooling the dielectric load is made through the ridges and the bottom-lid of the horn.

A. Excitation—Orthogonal Single-Ended Launch-Pins

The QRFH is fed with two orthogonal coaxial launch-pins for 50 Ω single-ended excitation. The launch-pins are made from standard 50 Ω semi-rigid cables (UT-047) where the outer conductor has been lathed off. The inner pin has a diameter of 0.287 mm with a surrounding PTFE dielectric with diameter specifications 0.94 ± 0.025 mm. The launch-pin is inserted in a ridge on one side of the horn and connected to a standard female SMA connector (Southwest: 214-500SF). In the opposite ridge the launch-pin is clamped with a claw-shaped chuck connector, see Fig. 5(c) and (d), to make electrical contact close to the hole in the ridge. A screw with a push-pin forces the chuck to contact the ridge from the inside. The chuck clamps the launch-pin as the hole in the ridge is chamfered on the inside to a diameter smaller than the 0.9 mm chuck diameter. In Fig. 5(a) and (b) the launch-pin with chuck connector and push-pin is laid out for overview. In Fig. 4(d) the launch-pin holes at the bottom of the horn are shown without SMA connectors. The offset for the two orthogonal launch-pins is 0.6 mm. In Fig. 5(e) the installed launch-pins are shown from the bottom of the QRFH. In Fig. 5(f) the dielectric load is clamped between the ridges with the launch-pins fed through it.

IV. Simulated and Measured Performance

In this section, the simulated data of the QRFH is compared to the measured. We present data for the QRFH without (w/o) and with (w/) the dielectric load installed. The beam patterns of the QRFH were measured in an anechoic far-field chamber. The transmitter antenna used was a ETS-Lindgren's (Model 3164-05) open boundary QRFH specified over 2–18 GHz and usable down to 1.5 GHz according to the manufacturer. Beam patterns are presented as co- and cross-polarization according to Ludwig's third definition [21]. The S-parameters were measured with a calibrated Agilent E8362C PNA specified over 10 MHz to 20 GHz. For the S-parameter analysis we present a tolerance study. The QRFH is also evaluated through simulation in an axisymmetric prime-focus $f/D = 0.3$ reflector for its intended radio astronomy application. The main properties of interest on the reflector is aperture efficiency with sub-efficiencies, sensitivity in terms of system equivalent flux density (SEFD), and intrinsic cross-polarization ratio (IXR).

A. Beam Patterns

Simulated and measured beam patterns agree well over the specified range of 1.5–15.5 GHz, see Fig. 9. Over the range of 1.5–2 GHz, the transmit antenna was not specified but usable, according to the manufacturer, which could explain the increased sidelobe level measured in E-plane for 1.5 GHz. Over the range of 5–15.5 GHz frequencies, a broader beamwidth is obtained in H-plane ($\phi = 90°$) with the dielectric load, Fig. 6(a), compared to without it, Fig. 6(b). Consequently this results in a broader D-plane ($\phi = 45°$) as well. The effect on E-plane beamwidth ($\phi = 0°$) is small for mid to upper frequencies, but slightly larger at the lower part of the band. In Fig. 7(a), the H-plane for 10 GHz is broadened $2 \times 6.5°$ at the -12 dB edge taper level due to the dielectric load. The cross-polarization discrimination (XPD) in D-plane, is improved by 4 dB at 10 GHz, as illustrated in Fig. 7(b).

For maximum gain calibration measurement, three 20 dB standard gain horns (SGH) were available at the facility, WR284 (2.60–3.95 GHz), WR187 (3.94–5.99 GHz), and WR90 (8.20–12.5 GHz). From the SGHs' specifications, an uncertainty to the gain measurement of ±0.5 dB was estimated. Due to difficulty in determining the exact phase center of the SGHs' relative the center of rotation in the

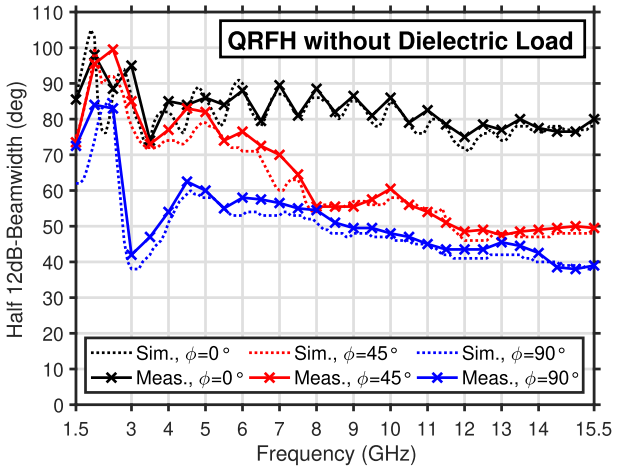

(a)

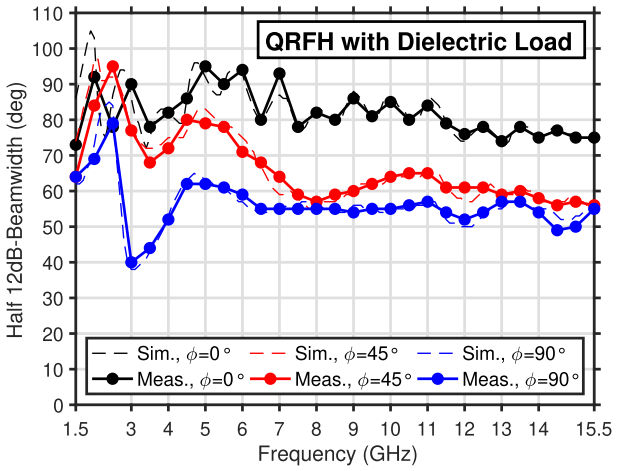

(b)

Fig. 6. Simulated and measured QRFH co-polarized half 12 dB beamwidth in planes $\phi = 0°$, 45°, 90° (a) without and (b) with the dielectric load.

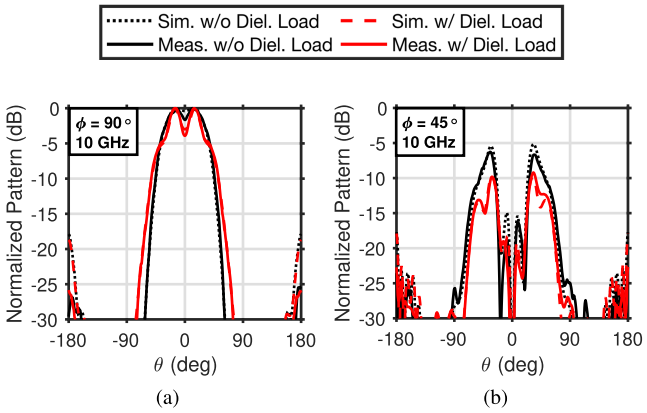

(a) (b)

Fig. 7. Simulated and measured QRFH beam pattern at 10 GHz without (w/o) and with (w/) the dielectric load. (a) Co-polarization in $\phi = 90°$. (b) Cross-polarization in $\phi = 45°$.

anechoic chamber, an additional error of ±0.25 dB was added. In Fig. 8 the measured gain is plotted with error bars to account for the mentioned uncertainties. The gain was only measured with the dielectric load installed in the QRFH.

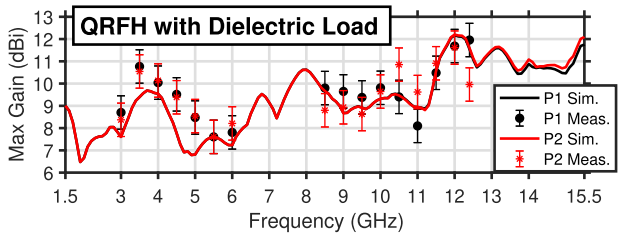

Fig. 8. Simulated and measured QRFH maximum gain for the two polarizations. Error of ±0.75 dB.

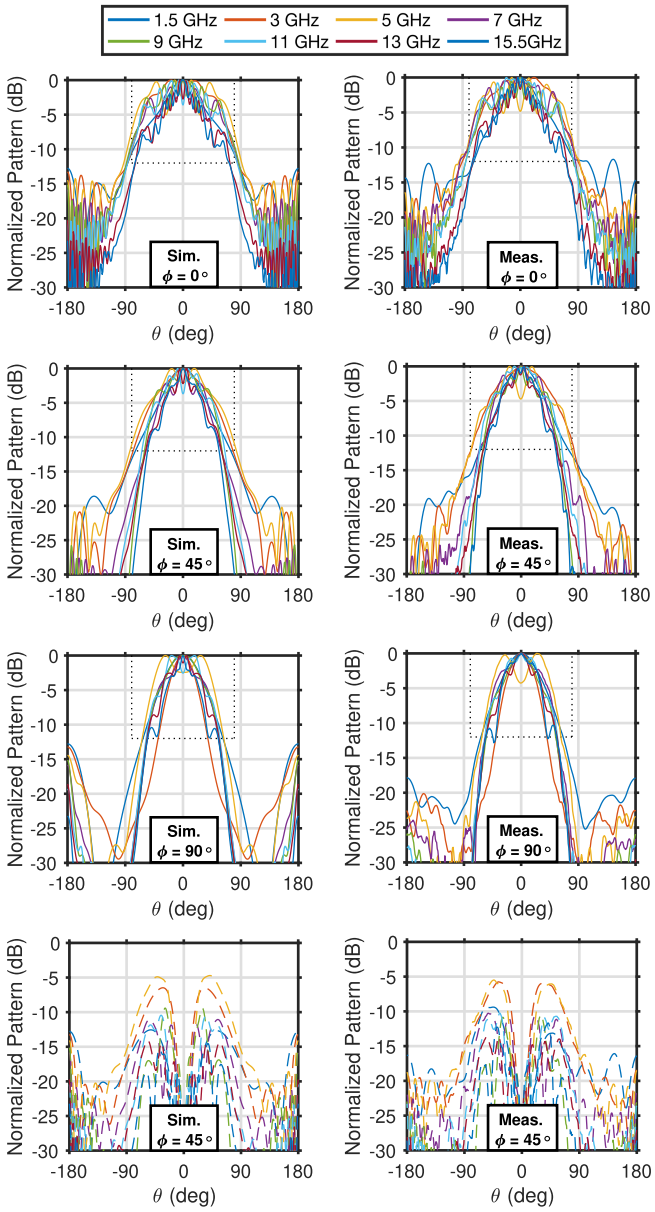

Fig. 9. Simulated (Left) and measured (Right) QRFH beam patterns with dielectric load over 1.5–15.5 GHz for planes $\phi = 0°$, 45°, 90°. Dotted rectangle represent −12 dB at $\theta_e = 79.6°$. Bottom-row is cross-polarization for $\phi = 45°$.

B. Aperture- and Sub-Efficiencies

In Fig. 10, the simulated aperture efficiency, η_a, with sub-efficiencies for the QRFH on a $f/D = 0.3$ prime-focus reflector is presented [20]. The location of the reflector focal

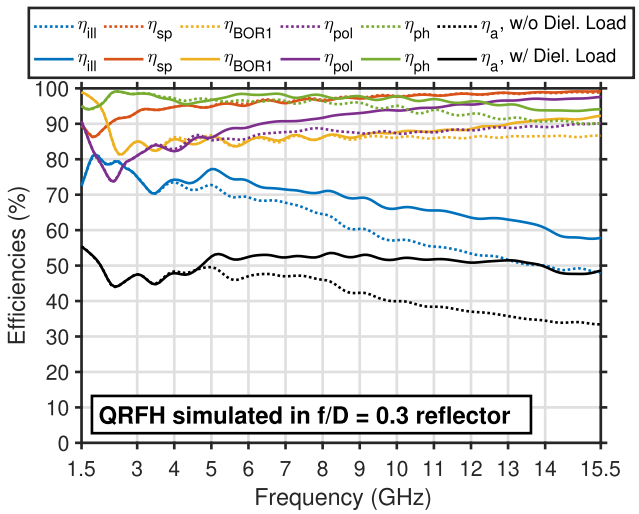

Fig. 10. Calculated efficiencies given as percentage for the QRFH without (w/o) and with (w/) the dielectric load in a prime-focus $f/D = 0.3$ reflector.

TABLE II

SIMULATED AVERAGE EFFICIENCIES (IN %) FOR THE QRFH IN A PRIME-FOCUS $f/D = 0.3$ REFLECTOR

	η_{ill}	η_{sp}	η_{BOR1}	η_{pol}	η_{ph}	η_a
w/o Diel. Load, 1.5–15.5 GHz	62.5	96.4	86.3	86.6	92.5	41.5
w/ Diel. Load, 1.5–15.5 GHz	68.8	96.3	87.7	90.8	96.6	50.6

point relative to the QRFH is chosen such that the highest average phase efficiency, η_{ph}, is achieved across 1.5–15.5 GHz. Without the dielectric, the best location is 38.5 mm inside the QRFH, and with the dielectric installed it is fixed to 36.5 mm inside. Both measured from the QRFH aperture. With the dielectric load, spill-over efficiency, η_{sp}, is above 95% for 79% of the band, and above 90% for 92% of the band. Below 3 GHz the reflector is over-illuminated which is consistent with the increased QRFH beamwidth at the low frequencies shown in Fig. 6(b). This causes η_{sp} to drop to 86% at the worst point. This, together with the low polarization efficiency, η_{pol}, in this region, causes the aperture efficiency to drop to its minimum of $\eta_{\text{a}} = 44\%$ at 2.4 GHz. It is clear from Fig. 10 that below 5 GHz, the radiating performance is dominated by the metallic QRFH structure with almost no effect from the dielectric load. The dielectric load improves η_{ph} with up to 4% from 5 GHz to 15.5 GHz, which implicates a more consistent phase center of mid and upper frequencies. The polarization efficiency is improved with up to 8% in the same frequency range and the azimuth-mode efficiency, η_{BOR1} is improved from 8.5 GHz and upward with up to 5.5% due to the dielectric load. Illumination efficiency, η_{ill}, is increased from mid to upper band with up to 11% because of the dielectric load, which corresponds to the broadening of the beam in Fig. 6(b). Peak aperture efficiency $\eta_{\text{a}} = 55\%$ together with an average of 50.6% across 1.5–15.5 GHz is an excellent result. In Table II average efficiencies over 1.5–15.5 GHz are summarized with (w/) and without (w/o) dielectric load. This performance is better than what has been achieved for previous QRFH designs for $f/D = 0.3$ which also have narrower bandwidths, see [22, pp. 78].

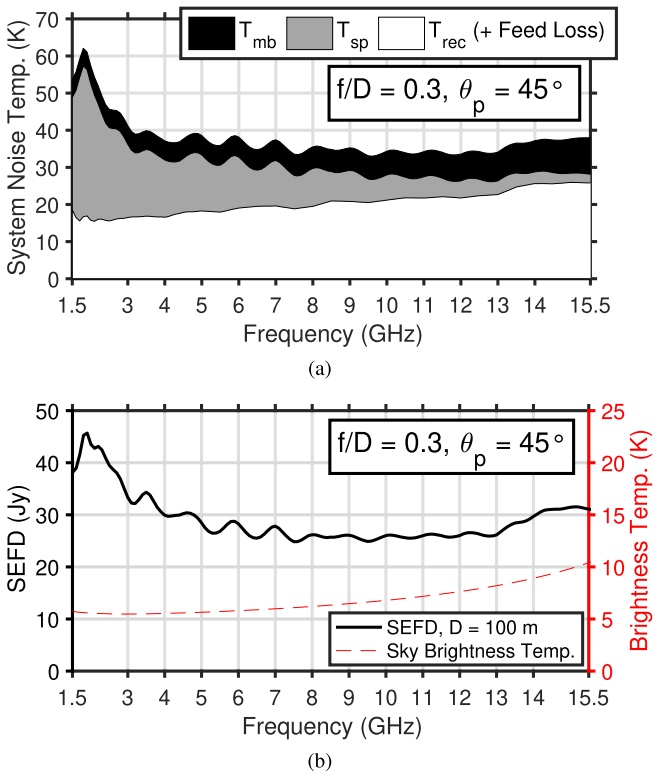

Fig. 11. Sensitivity of the dielectrically loaded QRFH calculated for a prime-focus $f/D = 0.3$ reflector with D = 100 m. (a) T_{sys}. (b) SEFD and sky brightness temperature, T_{sky}.

C. Sensitivity—System Equivalent Flux Density

For radio astronomy the figure-of-merit is the sensitivity, which here is given as SEFD. SEFD is defined as $2k_{\text{B}}(T_{\text{sys}}/A_{\text{eff}})$ where A_{eff} is the effective area illuminated on the reflector dish, T_{sys} the total system noise temperature and k_{B} the Boltzmann's constant. The effective area is calculated from the reflector main-beam gain, G, as $A_{\text{eff}} = (G\lambda^2)/(4\pi)$. To account for aperture blockage from the mechanical structure with struts, a 7% reduction of A_{eff} is included [23, pp. 180]. Total system noise temperature is calculated as $T_{\text{sys}} = \eta_{\text{rad}}T_{\text{a}} + (1 - \eta_{\text{rad}})T_{\text{phy}} + T_{\text{rec}}$, where η_{rad} is the antenna radiation efficiency, T_{a} the antenna noise temperature, T_{phy} the physical antenna temperature, and T_{rec} the receiver noise temperature including mismatches and the cryogenic LNAs. T_{a} can be calculated as the full-sphere integral of the surrounding brightness temperature weighted by the reflector beam pattern [24]. There are two main noise temperature contributions to T_{a}: Inevitable noise picked up by the main-beam from the sky brightness temperature, T_{sky}; Spill-over noise picked up from the ground temperature, T_{gnd}. In a prime-focus reflector, the feed is pointing toward the ground assuming the reflector points in zenith. Therefore, we approximate T_{a} using the spill-over efficiency as $T_{\text{a}} \approx \eta_{\text{sp}}T_{\text{sky}} + (1 - \eta_{\text{sp}})T_{\text{gnd}}$. Noise temperature picked up by the main-beam is represented by $T_{\text{mb}} = \eta_{\text{sp}}T_{\text{sky}}$ and the ground spill-over from the feed as $T_{\text{sp}} = (1 - \eta_{\text{sp}})T_{\text{gnd}}$. For an angle away from zenith, θ_p, the reflector main-beam points closer to the horizon and the spill-over picked up from the

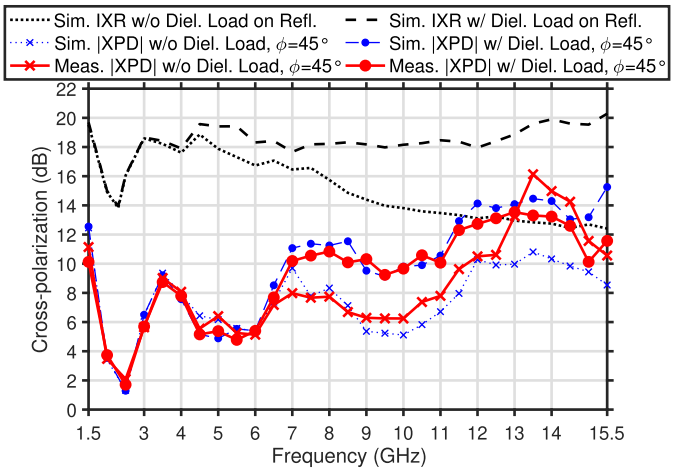

Fig. 12. Cross-polarization: |XPD| in $\phi = 45°$ for the QRFH, and minimum IXR within HPBW for the QRFH on a $f/D = 0.3$ reflector. Without (w/o) and with (w/) the dielectric load.

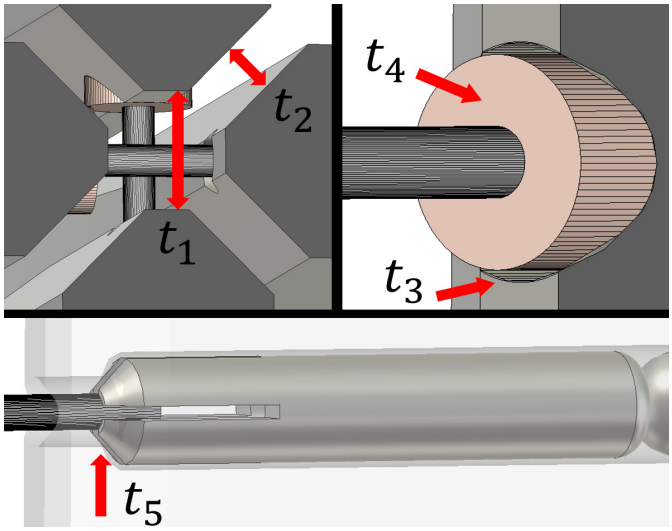

Fig. 13. Tolerances analyzed at the excitation point: t_1 and t_2 for ridge separation, t_3 and t_4 for diameter and length of the launch-pins' dielectric respectively, and t_5 for contact-point of the launch-pins inside the ridges. In the analysis, tolerances are given as deviations from nominal values, $\Delta t_1 \ldots \Delta t_5$.

ground would change. This is because more side-lobes could then potentially be terminated on the sky. The approximation of T_a, is still reasonable for a zenith angle of $\theta_p = 45°$. The receiver noise temperature, T_{rec}, at a physical temperature of 20 K is estimated from measured LNA data contributing with 8–13 K over the band, and additional 6–8 K from the other receiver components. Expected feed loss with the dielectric load is 0.12 to 0.24 dB over the band, which corresponds to a noise temperature increment of 2 to 4 K at a physical feed temperature of 70 K. In addition to T_{rec} a margin of 2 K for back-end and digitization noise is added to T_{sys}. T_{sky} is given from the general SKA brightness temperature model [24], which for 1.5–15.5 GHz is in the order of 6–11 K for zenith angle $\theta_p = 45°$. Calculated T_{sys} for $\theta_p = 45°$ is presented in Fig. 11(a) with the corresponding SEFD presented in Fig. 11(b). T_{sys} is between 35 and 63 K where T_{sp} contributes the most at lower frequencies. Due to high η_a over the decade bandwidth, SEFD is predicted between 24.8 and 45.6 Jy for a D =100 m reflector with $f/D = 0.3$. This sensitivity expressed as A_{eff}/T_{sys} would be 60.4–111.2 m^2/K.

D. Intrinsic Cross-Polarization Ratio

The feed's polarization purity calculated in a reflector system is represented by the IXR [25]. The IXR is independent of the coordinate system chosen and calculated from the maximum and minimum amplitude gain of the reflector beam pattern's Jones-matrix. For the wideband receivers of the SKA project [1], the minimum IXR (positive number) is required to be better than 15 dB within half-power beamwidth (HPBW). In Fig. 12, simulations of the QRFH on a 100 m $f/D = 0.3$ reflector, show improvement in IXR from 3.5 GHz and upward due to the dielectric load. The XPD (|XPD|) in $\phi = 45°$ (worst case) for the feed without reflector, is improved up to 4 dB. Over the frequency range 13–15 GHz, the measured |XPD| without dielectric load is better than simulated. The |XPD| is poor for the feed between 2 and 3 GHz due to degraded beam patterns, which also results in the lowest IXR of 14 dB. However, over most of the frequency band the simulated IXR with the dielectric load included, is better than the 15 dB limit set for SKA.

V. S-Parameters With Tolerance Analysis

The simulated input reflection coefficient of the QRFH with dielectric load, is below −10 dB over 1.5–15.5 GHz for both polarizations, see Fig. 14(a). At the low frequency end, the dielectric load gives a shaper cutoff just below 1.5 GHz. The simulated port isolation is better than 40 dB and the measured better than 35 dB for most of the band, as shown in Fig. 14(d). The measured input reflection coefficients, presented in Fig. 14(b) and (c), are higher than the simulated, both without and with the dielectric load. With the dielectric load installed, the highest measured S_{11} and S_{22} over 1.5–15.5 GHz is −7.5 and −7 dB respectively. From inspections of the manufactured components and the assembled QRFH, we have extracted five possible tolerance parameters that could explain the deviations between the simulated and measured results.

A. Tolerance Parameters

The five tolerance parameters investigated are: t_1, separation between opposite ridges; t_2, separation between adjacent orthogonal ridges; t_3, the diameter of the dielectric surrounding the launch-pins; t_4, the length of the dielectric surrounding the launch-pins (nominal is as long as the drilled hole); t_5, the contacting point of the launch-pin inside the ridge. In Fig. 13 these tolerance parameters are illustrated for clarity. In the analysis, the tolerances are presented as deviations, $\Delta t_1 \ldots \Delta t_5$, from nominal values. Without the dielectric load, the distance between opposite ridges and the distance between adjacent orthogonal ridges were both measured to be 0.15 mm larger than nominal separation. This separation was increased more due to the fact that the dielectric load has slightly more

positive tolerances (a bit larger) than nominal. This forces a slightly larger separation between the ridges when it is clamped in-between. The resulting tolerances was measured to be $\Delta t_1 = 0.3$ mm and $\Delta t_2 = 0.2$ mm, which is 25% and 40% larger than nominal separation, respectively. The holes for excitation launch-pins were drilled with a diameter of 1 ± 0.02 mm. Measurements of the launch-pins' dielectric showed a deviation from nominal diameter with the worst being $\Delta t_3 = -0.2$ mm ($=-20\%$ smaller than nominal). This alters the impedance match due to the air-gap that is created in the coaxial line. The launch-pins' dielectric length deviated $\Delta t_4 = \pm 0.25$ mm ($=\pm 2\%$) from nominal length due to the accuracy of cutting tools. This deviation results in that either the launch-pin dielectric extends outside the hole into the horn, or is slightly too short. For the nominal design, the chuck connector contacts the launch-pins 0.7 mm inside the ridges, which is indicated by the arrow in the bottom of Fig. 13. Measurements of the drilled hole depth indicated that the contact point was up to $\Delta t_5 = 1$ mm further inside the ridges than nominal (to the right of the arrow in Fig. 13). The deviation in contact point is strongly dependent on the accuracy of the chamfered section in the holes.

B. Tolerance Analysis

The tolerance simulations of the horn were only performed with the dielectric load included. In simulations, we first varied each tolerance parameter separately, $\Delta t_1 \ldots \Delta t_5$, within the corresponding interval presented in Section V-A. Second, we varied all five tolerance parameters simultaneously in random combinations within the presented intervals. From the simulated results where each tolerance parameter was varied separately, we analyzed their individual effects over the band. The range of 1.5–3 GHz was mostly affected by the separation between orthogonal adjacent ridges Δt_2. The range of 5–8 GHz was mostly affected by separation between opposite ridges Δt_1. Both Δt_1 and Δt_2 slightly degraded the performance in the range of 12–15.5 GHz, but the most severe degradation in this range was caused by the deviation in launch-pin contact point Δt_5. The diameter of the dielectric surrounding the launch-pins corresponds to Δt_3 and it had an effect of a few decibels over the band on the input reflection coefficients. Δt_4 representing length of the launch-pin's surrounding dielectric, only has a small effect overall.

From the simulated results where all five parameters were varied simultaneously in random combinations within the presented intervals, the best and worst limit of the input reflection coefficients and the isolation were extracted. These limits constitute the blue error bars for the simulated S-parameters in Fig. 14(b)–(d). The measured input reflection coefficients (thick red curves = measured w/ diel. load) are mostly within these simulated error bars. This indicates that the tolerances of the manufactured components are within the intervals that were simulated in the analysis. For the isolation, Fig. 14(d), additional effects should be included such as potential asymmetry at the excitation point caused by slightly misaligned launch-pins. This is not accounted for in the simulations, but could further degrade the isolation.

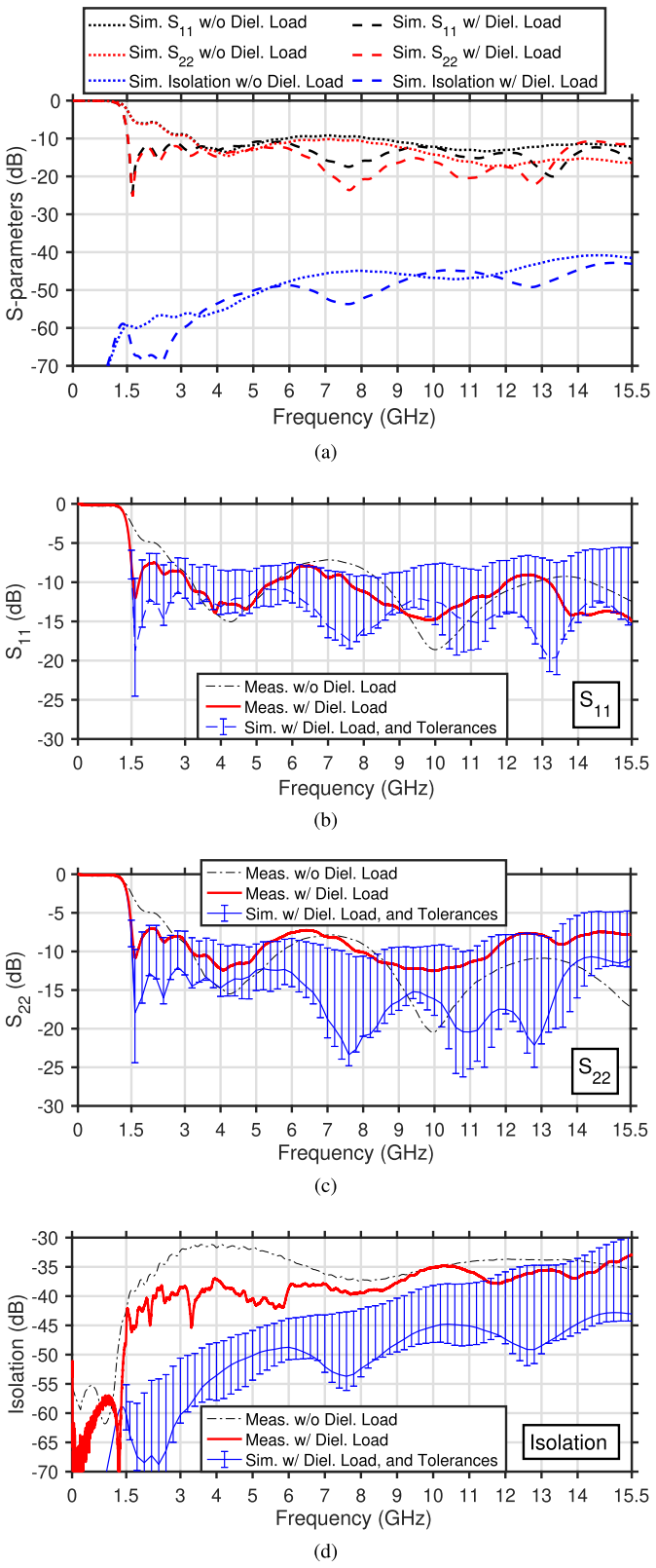

Fig. 14. S-parameters for the QRFH. Nominal simulated in (a). Simulated with tolerances compared to measured in (b) S_{11} (Port 1), (c) S_{22} (Port 2), and (d) Isolation (S_{21} or S_{12}).

From the analysis presented where each of the tolerance parameters were varied separately in simulation, we can interpret the measured results. The measured S_{22} was degraded

TABLE III
ACCEPTABLE TOLERANCES FOR MANUFACTURING

Δt_1	Δt_2	Δt_3	Δt_4	Δt_5
± 0.1 (mm)	± 0.05 (mm)	-0.1 (mm)	± 0.25 (mm)	$+0.3$ (mm)

more than the measured S_{11} when the dielectric load was installed compared to without it, see Fig. 14(b) and (c). From the tolerance simulations, this degradation over 3–8 GHz indicates that the separation is slightly larger between the opposite ridges and adjacent orthogonal ridges for the second polarization (S_{22}) than for the first (S_{11}). This indicates that the machined traces of the dielectric load for the second polarization is slightly more positive than for the first. The measured degradation of S_{22} over 12–15.5 GHz compared to S_{11}, indicates that the contact point is further inside the ridge for the second polarization than for the first.

In this tolerance analysis, only larger deviations than nominal were presented for the separation between ridges as this was shown in simulation to have the worst effect and was what we observed in measurement. For the launch-pin contact point, a location to the left of the arrow in Fig. 13 would not degrade the input reflection coefficients and is therefore not included here.

C. Tolerances for Production

From the simulated results when all the five tolerance parameters were varied simultaneously and randomly, we extracted new tolerance intervals within which the input reflection coefficients were below -10 dB over 1.5–15.5 GHz. These intervals were again simulated, with Δt_1 and Δt_2 now also allowed to be negative, as could be the case in production. The new tolerance intervals are presented in Table III and are specified to give input reflection coefficients below -10 dB over 1.5–15.5 GHz. The most important tolerance parameters are the separation between opposite ridges, the separation between orthogonal adjacent ridges, and the contact point in the ridges for the launch-pins. The separation between adjacent orthogonal ridges should have the strictest tolerance requirement. To achieve these tolerances, the machined profile of the ridge and the traces from the ridges in the dielectric load should be specified appropriately before manufacturing. The same applies for the drilled hole depth toward the chamfer inside the ridge and the dimensions of the machined chuck-connector.

VI. CONCLUSION

In this article we have presented the design, manufacture and performance of a dielectrically loaded QRFH over 1.5–15.5 GHz for radio astronomy application over decade bandwidth. The dielectric load is machined from low-loss homogeneous PTFE and has a simple shape that is clamped between ridges of the horn and the back-short. The low profile of the dielectric load keeps the QRFH compact which is important when integrated in a cryostat dewar. The dielectric load gives a more stable beamwidth in the feed H-plane pattern over frequency. Consequently, the illumination and phase efficiency for the feed simulated on a reflector are improved over mid and upper frequencies due to the dielectric load. The resulting aperture efficiency fulfills the BRAND project's goal with an average of $\eta_a = 50\%$ across the decade bandwidth. Simulated intrinsic cross-polarization is better than 15 dB for most of the frequency band. SEFD for radio astronomy is calculated on a 100 m reflector to be 24.8–45.6 Jy over the band. Spill-over efficiency is above 90% over 92% of the bandwidth. The measured beam patterns of the QRFH agree well with simulations over the full bandwidth. Measured port isolation is better than 35 dB for most of the band. Input reflection coefficients are predicted in simulations to be below -10 dB over the bandwidth. The highest measured input reflection coefficient is -7 dB. We present a tolerance analysis of the QRFH excitation point that explains this deviation. We also provide acceptable tolerance intervals for production to achieve nominal input reflection coefficient.

ACKNOWLEDGMENT

The authors would like to thank J. Yang for improving this manuscript and S. M. Moghaddam for assisting in the beam pattern measurements, both are with the Department of Electrical Engineering, Chalmers University of Technology, Gothenburg, Sweden. They would also like to thank L. Helldner, R. Wingdén, and M. Dahlgren are with the Onsala Space Observatory, Onsala, Sweden, and L. Steponavicius is with MegaMETA, Lithuania for advice during manufacturing.

REFERENCES

[1] P. E. Dewdney, W. Turner, R. Millenaar, R. McCool, J. Lazio, and T. J. Cornewell. (Mar. 2013). *SKA1 System Baseline Design (SKA-TEL-SKO-DD-001)*. [Online]. Available: https://www.skatelescope.org/wp-content/uploads/2012/07/SKA-TEL-SKO-DD-001-1_BaselineDesign1.pdf

[2] W. J. Welch *et al.*, "New cooled feeds for the allen telescope array," *Publications Astronomical Soc. Pacific*, vol. 129, no. 974, Mar. 2017, Art. no. 045002.

[3] M. McKinnon, C. Carilli, and T. Beasley, "The next generation very large array," *Proc. SPIE*, vol. 9906, Jul. 2016, Art. no. 990627.

[4] G. Tuccari *et al.*, "BRAND: A very wide-band receiver for the EVN," in *Proc. 23rd Eur. Very Long Baseline Interferometry Group Geodesy Astrometry*, Gothenburg, Sweden, May 2017, pp. 81–83.

[5] J. Flygare, M. Pantaleev, and S. Olvhammar, "BRAND: Ultra-wideband feed development for the European VLBI network—A dielectrically loaded decade bandwidth quad-ridge flared horn," in *Proc. 12th Euro. Conf. Antennas Propag. (EuCAP)*, London, U.K., Apr. 2018, p. 5.

[6] R. Lehmensiek and I. P. Theron, "*L*-band feed horn and orthogonal mode transducer for the KAT-7 radio telescope," *IEEE Trans. Antennas Propag.*, vol. 59, no. 6, pp. 1894–1901, Jun. 2011.

[7] J. Schleeh *et al.*, "Cryogenic 0.5–13 GHz low noise amplifier with 3 K mid-band noise temperature," in *IEEE MTT-S Int. Microw. Symp. Dig.*, Montreal, QC, Canada, Jun. 2012, pp. 15–17.

[8] N. Wadefalk *et al.*, "Cryogenic wide-band ultra-low-noise IF amplifiers operating at ultra-low DC power," *IEEE Trans. Microw. Theory Techn.*, vol. 51, no. 6, pp. 1705–1711, Jun. 2003.

[9] J. Yang *et al.*, "Cryogenic 2–13 GHz eleven feed for reflector antennas in future wideband radio telescopes," *IEEE Trans. Antennas Propag.*, vol. 59, no. 6, pp. 1918–1934, Jun. 2011.

[10] J. Yang, M. Pantaleev, P.-S. Kildal, and L. Helldner, "Design of compact dual-polarized 1.2–10 GHz eleven feed for decade bandwidth radio telescopes," *IEEE Trans. Antennas Propag.*, vol. 60, no. 5, pp. 2210–2218, May 2012.

[11] G. Cortes-Medellin, "Non-planar quasi-self-complementary ultra-wideband feed antenna," *IEEE Trans. Antennas Propag.*, vol. 59, no. 6, pp. 1935–1944, Jun. 2011.

[12] A. Akgiray, S. Weinreb, W. A. Imbriale, and C. Beaudoin, "Circular quadruple-ridged flared horn achieving near-constant beamwidth over multioctave bandwidth: Design and measurements," *IEEE Trans. Antennas Propag.*, vol. 61, no. 3, pp. 1099–1108, Mar. 2013.
[13] T. S. Beukman, P. Meyer, M. V. Ivashina, and R. Maaskant, "Modal-based design of a wideband quadruple-ridged flared horn antenna," *IEEE Trans. Antennas Propag.*, vol. 64, no. 5, pp. 1615–1626, May 2016.
[14] J. Shi, S. Weinreb, W. Zhong, X. Yin, and M. Yang, "Quadruple-ridged flared horn operating from 8 to 50 GHz," *IEEE Trans. Antennas Propag.*, vol. 65, no. 12, pp. 7322–7327, Dec. 2017.
[15] A. Dunning, M. Bowen, M. Bourne, D. Hayman, and S. L. Smith, "An ultra-wideband dielectrically loaded quad-ridged feed horn for radio astronomy," in *Proc. IEEE-APS Top. Conf. Antennas Propag. Wireless Commun. (APWC)*, Turin, Italy, Sep. 2015, pp. 787–790.
[16] B. Dong, J. Yang, J. Dahlström, J. Flygare, M. Pantaleev, and B. Billade, "Optimization and realization of quadruple-ridge flared horn with new spline-defined profiles as a high-efficiency feed from 4.6 GHz to 24 GHz," *IEEE Trans. Antennas Propag.*, vol. 67, no. 1, pp. 585–590, Jan. 2019.
[17] T. Satoh, "Dielectric-loaded horn antenna," *IEEE Trans. Antennas Propag.*, vol. AP-20, no. 2, pp. 199–201, Mar. 1972.
[18] R. J. Bauerle, R. Schrimpf, E. Gyorko, and J. Henderson, "The use of a dielectric lens to improve the efficiency of a dual-polarized quad-ridge horn from 5 to 15 GHz," *IEEE Trans. Antennas Propag.*, vol. 57, no. 6, pp. 1822–1825, Jun. 2009.
[19] B. Billade, J. Flygare, M. Dahlgren, and B. Wästberg, and M. Pantaleev, "A wide-band feed system for SKA band 1 covering frequencies from 350–1050 MHz," in *Proc. 10th Euro. Conf. Antennas Propag. (EuCAP)*, Davos, Switzerland, Apr. 2016, pp. 1–3.
[20] P.-S. Kildal, "Factorization of the feed efficiency of paraboloids and cassegrain Antennas," *IEEE Trans. Antennas Propag.*, vol. AP-33, no. 8, pp. 903–908, Aug. 1985.
[21] A. Ludwig, "The definition of cross polarization," *IEEE Trans. Antennas Propag.*, vol. 21, no. 1, pp. 116–119, Jan. AP-1973.
[22] A. H. Akgiray, "New technologies driving decade-bandwidth radio astronomy: Quad-ridged flared horn and compound-semiconductor LNAs," Ph.D. dissertation, California Inst. Technol., Pasadena, CA, USA, 2013. [Online]. Available: http://thesis.library.caltech.edu/7644/
[23] T. L. Wilson, K. Rohlfs, and S. Hüttemeister, *Tools of Radio Astronomy*, 6th ed., A. Library, Ed. Cham, Switzerland: Springer, 2013.
[24] G. Cortes-Medellin. (Jul. 2007). *MEMO 95 Antenna Noise Temperature Calculation*. [Online]. Available: https://www.skatelescope.org/uploaded/6967_Memo_95.pdf
[25] T. D. Carozzi and G. Woan, "A fundamental figure of merit for radio polarimeters," *IEEE Trans. Antennas Propag.*, vol. 59, no. 6, pp. 2058–2065, Jun. 2011.

Jonas Flygare (S'16) was born in Mölndal, Sweden, in 1988. He received the B.Sc. and M.Sc. degrees in engineering physics and the Licentiate degree from the Chalmers University of Technology, Gothenburg, Sweden, in 2016 and 2018, respectively. He is currently pursuing the Ph.D. degree in radio and space science with the Chalmers University of Technology.

In 2012, he was a Test Technician in semiconductor research and development with CBRITE Inc., Goleta, CA, USA, where he was developing the thin-film-transistor technology for next-generation flat screens. In 2014, he was with the Department of Electrical Engineering, Chalmers University of Technology, where he was working with the gap-waveguide technology. From 2014 to 2016, he was a Project Researcher with the Onsala Space Observatory, Gothenburg, Swedish National Facility for Radio Astronomy, where he was involved to design the feed antenna for the Square Kilometer Array (SKA) Band 1 in radio astronomy. His current research interests include design and system characterization of ultra-wideband antennas and reflector feeds, low-noise amplifiers, phased arrays feeds, and receivers for radio and millimeter wave applications in radio astronomy.

Mr. Flygare received the TICRA Travel Grant by the IEEE APS/URSI, Boston, MA, USA, in 2018.

Miroslav Pantaleev received the M.Sc. degree in radio communications from Sofia Technical University, Sofia, Bulgaria, in 1995, and the M.Sc. degree in digital communications and the Ph.D. degree from the Chalmers University of Technology, Gothenburg, Sweden, in 2000 and 2006, respectively.

From 2006 to 2018, he was the Leader of the Electronics Laboratory, Onsala Space Observatory, Gothenburg, Swedish National Facility for Radio Astronomy, where he was involved in the development of millimeter-wave receivers for applications in radio astronomy and space sciences. Instruments designed by him are currently in operation at the Atacama Pathfinder Experiment Telescope and the Onsala Space Observatory. Since 2012, he has been leading the Swedish technical involvement in the Square Kilometer Project (SKA). His team delivered the design and the prototype of one of the receivers to be installed on the 15 m reflector antennas of the SKA telescope. Since 2018, he has been with the RUAG Space, Zürich, Switzerland, where he is currently the Team Leader of the Electrical Engineering Group. His current research interest includes space electronics and antennas.